`

Motion Estimation for a Compact Electrostatic Micro-scanner via Shared Driving and Sensing Electrodes in Endomicroscopy

Yi Chen, Miki Lee, Mayur Bhushan Birla, Haijun Li, Gaoming Li,
Xiyu Duan, Thomas D. Wang, Kenn R. Oldham

***Abstract*—We present a method to estimate high frequency rotary motion of a highly compact electrostatic micro-scanner using the same electrodes for both actuation and sensing. The accuracy of estimated rotary motion is critical for reducing blur and distortion in image reconstruction applications with the micro-scanner given its changing dynamics due to perturbations such as temperature. To overcome the limitation that no dedicated sensing electrodes are available in the proposed applications due to size constraints, the method adopts electromechanical amplitude modulation (EAM) to separate motion signal from parasitic capacitance feedthrough, and a novel non-linear measurement model is derived to characterize the relationship between large out-of-plane angular motion and circuit output. To estimate motion, an extended Kalman filter (EKF) and an unscented Kalman filter (UKF) are implemented, incorporating a process model based on the micro-scanner's parametric resonant dynamics and the measurement model. Experimental results show that compared to estimation without using the measurement model, our method is able to improve the rotary motion estimation accuracy of the micro-scanner significantly, with a reduction of root-mean-square error (RMSE) in phase shift of 86.1%, and a reduction of RMSE in angular position error of 78.5 %.**

***Index Terms*—MEMS scanner, sensor modeling, extended Kalman filter, unscented Kalman filter, dynamic modeling**

I. Introduction

With the continuing development of microelectromechanical system (MEMS) technology, MEMS scanners have been used in an array of applications involving laser scanning and displays [1]. One interesting application is to use MEMS scanners in endomicroscope instruments [2], such as confocal endomicroscopes [3] or multiphoton endomicroscopes [4], replacing bulky conventional counterparts such as scanning mirror galvanometers [5].

MEMS scanners can be classified by their actuation principles into four main categories: electrostatic, electromagnetic, piezoelectric and electrothermal. Among these categories, the electrostatic micro-scanner uses the attractive forces generated by two oppositely charged plates or electrodes to rotate a mirror for directional laser scanning. Compared to other actuation principles, electrostatic actuators have advantages of comparatively straightforward fabrication and integration into microscopy systems, and therefore comprise the majority of endomicroscope scanners in the literature [1].

For high resolution and large field-of-view (FOV) imaging application, these scanners must achieve large deflection angles, and therefore are designed to have high quality factor and be operated at or near resonant frequencies [5]. As a result, this type of scanner suffers from resonance shift due to material property variation (density, thermal expansion, Poisson's ratio and elastic constants) and thermal expansion mismatch (due to usage of multilayer structures consisting of different materials) caused by temperature perturbation or other environmental changes [6]. Such a resonance shift will introduce error in phase and amplitude information to be used in the image reconstruction process. Without appropriate image processing, incorrect phase information will lead to blurred images due to misplaced pixels while incorrect amplitude information will lead to distorted images.

One solution to this issue is to provide accurate phase and amplitude estimation of the rotary motion using on-chip sensing. Previous works have combined electrostatic actuation with various on-chip sensing mechanisms including piezoresistive sensing [7], piezoelectric sensing [8] [9], and capacitive sensing [5]. However, all of these designs require extra space on-chip and increase the number of electrical interconnects needed between the instrument and control circuitry, both of which are difficult to accommodate in small endomicroscopy instruments (2.4 to 5 mm in diameter) [2]. Therefore it is desired to reduce the device size by combining the driving and sensing capacitor into one set of electrodes. Such design efforts, however, lead to larger feedthrough disturbances between driving voltage inputs and sensor outputs due to shared electrodes and parasitic capacitances in all of the above sensing schemes. Hence, this study aims to seek an effective method to extract meaningful feedback signal while

This work was supported in part by the National Institutes of Health (Grant 5-R01-EB-020644) and the National Science Foundation (Grant CMMI 1334340). (*Corresponding author: Yi Chen.* e-mail: davidsky@umich.edu)

Y. Chen was with University of Michigan, Ann Arbor, MI 48109, USA. He is currently with Midea ETC, 250 W Tasman Dr, Suite 190, San Jose, CA 95134, USA.

M. Birla and K. R. Oldham are with the Department of Mechanical Engineering, University of Michigan, Ann Arbor, MI 48109, USA.

M. Lee, H. Li, G. Li and T. D. Wang are with the Department of Biomedical Engineering, University of Michigan, Ann Arbor, MI 48109, USA.

X. Duan was with University of Michigan, Ann Arbor, MI 48109, USA. He is currently with Apple Inc., Cupertino, CA 95014, USA.

reject disturbances, and estimate the rotary motion as accurate as possible with obtained signal.

Our prior studies have shown it is possible to perform high accuracy motion estimation with non-linear capacitance sensor models using dedicated capacitive electrodes. The feedthrough disturbance can either be eliminated by taking the difference of sensing signals from repetitive measurements with and without applying bias voltages [10] [11] or by purposely interrupting the device's driving voltage [12] [13]. Those methods however cannot be directly applied in the configuration in this study.

A common technique to reject feedthrough is to use electromechanical amplitude modulation (EAM), which employs an AC carrier at high frequency to perform amplitude modulation of the low frequency motion signal, and allows for separation of the motion signal and driving voltage feedthrough in the frequency domain with carefully designed filters [14]. [14] and [15] showed such techniques can be employed on sensing capacitors separated from driving capacitors. However very large frequency separations are required for use on a device using the same electrodes for both sensing and driving, and not necessarily applicable as mechanical motion frequency increases, as in this study.

Related to the use of electrostatic actuation and sensing with the same electrodes, a bi-axial micro-scanner is reported in [16], and the sensing signal was used in a phase-locked loop to ensure that the device would consistently be operated at resonance of its fast axis. A closed-loop controller for the scanner's slow axis was demonstrated subsequently in [17]. However, those works did not explicitly formulate a model between scanner's rotary motions to sensing signal, which would permit state estimation across the full range of tilting motion. Such modeling effort can be beneficial in building an estimator to estimate scanner motion for tracking and feedback control applications.

In this study, we present a method for high-accuracy motion estimation for an electrostatic micro-scanner with the same electrodes used for both sensing and driving. It employs a dedicated amplitude modulation-demodulation (AMDM) circuit to perform EAM and extract meaningful sensing signal in the presence of feedthrough. A novel non-linear measurement model is derived to characterize relation between large out-of-plane angular motion and circuit output. Then the motion estimation can be accomplished by EKF or UKF incorporating a process model based on parametric resonant scanner dynamics and the measurement model.

The presented estimation scheme is the most comprehensive for electrostatic micro-scanner rotary motion estimation in endomicroscopic laser-scanning applications relative to the literature. Specifically, we summarize our contribution as following:

- To propose a non-linear model to characterize the large amplitude rotary motion to an AMDM sensing circuit output for a compact electrostatic micro-scanner using electrodes for both sensing and driving. The modeling of the nonlinear capacitance function and demodulation process with envelope detector and analysis of frequency bands given close spacing of driving and sensing frequencies due to the fast mirror response has not been fully addressed in the past.
- To analyze theoretical effectiveness of EAM on separating motion signal and feedthrough disturbance generated by electrodes shared for sensing and driving in the above model. To implement and experimentally validate an EKF and an UKF incorporating single-axis electrostatic micro-scanner dynamics and the proposed measurement model.

The paper is organized as following: in Section II, the target and the method to achieve motion estimation are presented. Then the experimental set-up and procedures are described in Section III. In Section IV, the method for system identification and the estimators performance are discussed. Finally, a concluding remark is presented in Section V.

II. METHODS

A. Image registration and target of phase estimation

Since the goal of scanner motion estimation is to track potential phase shift of scanner motion and therefore to improve image registration, we first derive the target accuracy for phase estimation based on the relationship between the phase and image registration.

For simplicity, we examine the target phase shift accuracy of a one-dimensional image registered by scanning a line on an object. The FOV of an image can be parameterized by x such that $x = 0$ and $x = 1$ are extremes of the given FOV. In an imaging system with Lissajous laser scanning, the discrete locations $x(i)$ at which the object is sampled are described by

$$x(i) = \sin\left(2\pi f_{res}\frac{i}{f_s} + \phi^0\right) + 0.5 \tag{1}$$

where f_{res} is the mechanical resonant frequency of the scanner, f_s is sampling frequency, ϕ^0 is the phase difference between an applied periodic input voltage and resulting scanner motion. The intensity values from the object at sampling locations given by (1) are recorded to a vector $I_o(i)$. The 1D image ($2m$ pixels long) of a line scan can be reconstructed if one can map the intensity values $I_o(i)$ to corresponding pixel index k, accurately. The pixel index k can be computed by

$$k = \lceil 2mx(i) \rceil = \lceil m\sin(\psi(i) + \phi^0) \rceil + m \tag{2}$$

where m is half number of pixels in one dimension, $\lceil\ \rceil$ represents the least integer (or ceiling) function, and $\psi(i) = 2\pi f_{res}\frac{i}{f_s}$.

The image quality degrades when the phase drifts to $\phi^0 + \delta\phi$ and image is still reconstructed assuming phase of ϕ^0. This causes pixels to be associated with incorrect indices and leads to the blurry of the reconstructed image. Denoting the phase error as , the actual pixel index is expressed as:

$$k_{real} = \lceil m\sin(\psi(i) + \phi^0 + \delta\phi) \rceil + m. \tag{3}$$

Then the pixel shift δk can be defined as:

$$\delta k = k_{real} - k \tag{4}$$

Thus, maintaining an acceptable level of pixel shift (δk) dictates the target accuracy of phase angle estimation. Denoting the acceptable pixel shifting to be index p ($\delta k \le p$), produced by corresponding phase shift error $\delta\phi_p$, then using eq (2) – (4), δk can be written as

`

$$\delta k = \lceil m\sin(\psi(i) + \phi^0 + \delta\phi_p)\rceil - \lceil m\sin(\psi(i) + \phi^0)\rceil \quad (5)$$

It can be shown that δk is maximum when $\psi(t) \approx n\pi$; $n \in \mathbb{N}_0$, for small values of $\delta\phi_p$. By linearizing the sine term and using the property of least integer functions, we have

$$\delta k = m\delta\phi_p \leq p \quad (6)$$

This results in an upper bound on $\delta\phi_p$ given p and m

$$\delta\phi_p \leq p/m \quad (7)$$

A similar analysis can be performed for backward shifting and further extended for multi-axis scanners.

The above derivation is used to define a target phase estimation accuracy given image specifications. For instance, with an endomicroscope with resolution corresponding to 300 ×300 pixels (i.e. m = 150) and a target shift of pixel index p = 1, the required upper bound of $\delta\phi_p \leq \frac{1}{150} rad \approx 0.38$ deg.

B. Micro-scanner dynamics and process model

The electrostatic micro-scanner used in this study is a single-axis scanner as shown in Fig. 1. Multiple groups of comb-fingers are incorporated to generate electrostatic force and rotate the scanner under external voltage excitation. To minimize voltage requirements and external connections, all stator comb fingers are connected to the same voltage source, and all rotor (mirror) fingers are connected to ground. As previously shown in [18], out-of-plane motion is only generated near integer multiples of the natural frequency of free vibration for a planar structure, operated via parametric resonance.

The governing equation for torsional force acting on the mirror structure in rotational operation is:

$$T(t) = \frac{1}{2}\frac{dC_s(t)}{d\theta}V(t)^2 \quad (8)$$

where C_s is the total capacitance formed by the comb-fingers (not including parasitic capacitance), θ is the tilting angle of the micro-scanner and V is the driving voltage. The equation of motion of the scanner is described as:

$$J\ddot{\theta} + b\dot{\theta} + k\theta = \frac{1}{2}\frac{dC_s(t)}{d\theta}V(t)^2 \quad (9)$$

where J is the moment of inertia in rotation, b is damping coefficient, and k is the torsional spring constant of the device.

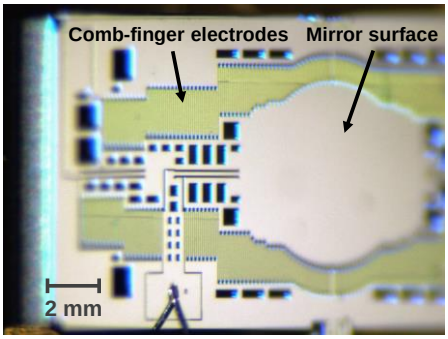

Fig. 1. A single-axis electrostatic micro-scanner used in this study. The comb-finger electrodes are used for both driving and sensing purpose.

Defining states $x_1 = \theta$ and $x_2 = \dot{\theta}$, defining $C_s' = dC_s/d\theta$, and denoting the sampling interval as T_s, (9) can be discretized with a first order Taylor expansion as:

$$\begin{bmatrix} x_{1,k} \\ x_{2,k} \end{bmatrix} = \begin{bmatrix} x_{1,k-1} + T_s x_{2,k-1} \\ -\frac{T_s k^2}{J^2}x_{1,k-1} + \left(1 - \frac{T_s b}{J}\right)x_{2,k-1} + \frac{T_s C_k'}{2J}V_k^2 \end{bmatrix} \quad (10)$$

where the subscript k stands for the k-th sampling instance in the discretized time domain. Assuming the process is corrupted by additive zero mean, normally distributed process noise $\boldsymbol{w_k}$, and letting $\boldsymbol{X_k} = [x_{1,k} \quad x_{2,k}]^T$, (5) can be represented as

$$\boldsymbol{X_k} = g(\boldsymbol{X_{k-1}}, V_k) + \boldsymbol{w_k} \quad (11)$$

where $g(\cdot)$ denotes the process model. We denote the covariance matrix of w_k as $\boldsymbol{Q}$, which after discretization is

$$\boldsymbol{Q} = Q_\theta \begin{bmatrix} \frac{1}{4}T_s^4 & \frac{1}{2}T_s^3 \\ \frac{1}{2}T_s^3 & T_s^2 \end{bmatrix} \quad (12)$$

where Q_θ is the noise variance of angular position.

C. Sensing principle and measurement model

Since C_s is a function of θ, the same comb-fingers used to produce electrostatic force for actuation can be used as angular position sensors. In this study, an AMDM circuit was designed and implemented to provide amplitude-modulated voltage to drive the electrostatic mirror near its resonant frequency and to demodulate the sensing signal associated with the tilting motion of the scanner.

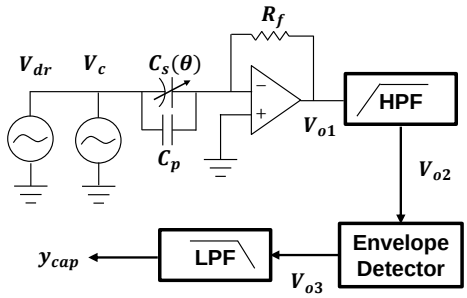

Fig. 2. Schematic of AMDM circuit used for driving and sensing with the electrostatic micro-scanner. The input voltage V_{dr} is modulated by a carrier voltage V_c and fed into the scanner. The current generated by the rotary motion of sensing capacitance $C_s(\theta)$ and the feedthrough by the parasitic capacitance C_p are processed by an amplification stage, a HPF stage, an envelope detector and a LPF stage subsequently, and is measured as y_{cap}.

Fig. 2 depicts the schematic of the AMDM circuit. It consists of an amplification stage, a high pass filter stage, an envelope detector and a low pass filter stage. The voltage outputs after each stage are noted as V_{o1}, V_{o2}, V_{o3}, y_{cap}, respectively.

To simplify measurement model derivation, two assumptions have been made: first, the parasitic capacitance is modeled as an additive capacitor, C_p, in parallel with C_s; second, since the operating frequency of the electrostatic scanner is almost always near its resonance, phase shifts introduced by the circuitry (low-pass and high-pass filters) are assumed to be constant and can be calibrated during initial experiments.

`

Firstly, $C_s(\theta)$ due to the rotary motion can be modeled with a Gaussian-like function,

$$C_s(\theta) = C_0 e^{-\left(\frac{\theta}{\theta_0}\right)^2} + C_b \quad (13)$$

where C_0 is the nominal capacitance, C_b is a fixed capacitance bias and θ_0 is the nominal angular displacement. This model has been shown to characterize capacitance over large range of angular motion quite effectively [18].

However, to analyze the frequency bands of the signal induced by the driving voltage and the oscillation of the capacitor, the Gaussian function can be overly complex. Therefore, a quadratic form of capacitance model simplified by neglecting the higher-order terms in the Taylor expansion of (13) is introduced:

$$C_s(\theta) = C_0\left(1 - \left(\frac{\theta}{\theta_0}\right)^2 + \frac{1}{2!}\left(\frac{\theta}{\theta_0}\right)^4 - \frac{1}{3!}\left(\frac{\theta}{\theta_0}\right)^6 + \cdots\right) + C_b \quad (14)$$

For motion $|\theta| \le \theta_0$, we approximate (14) by neglecting terms with order higher than 4, and then the sensing capacitance, C_s is modeled as quadratic function of θ,

$$C_s(t) = a_c\theta(t)^2 + b_c \quad (15)$$

where $a_c = -\frac{C_0}{\theta_0^2}$ is the scale factor of the capacitance model and $b_c = C_0 + C_b$ is the static capacitance of the capacitance model.

It should be pointed out that the replacement of a Gaussian model with a quadratic function is for the purpose of derivation of measurement model. Such replacement is valid for modest displacements as it is based on the observation that the capacitance profile of a comb-finger is symmetric about θ and thus can be modeled by even number of order of polynomials [19]. At the end of the derivation of the measurement model, we will review this assumption again and return to the model defined in (13) for the rest of the discussion.

As the EAM technique is implemented using a summing amplifier, the input voltage V to the scanner's comb-finger electrodes is composed of a driving voltage and a carrier voltage, and is expressed as:

$$V(t) = V_{dr0}\sin(\omega_{dr}t) + V_{c0}\sin(\omega_c t) \quad (16)$$

where V_{dr0} is the amplitude of driving voltage, ω_{dr} is the frequency of driving voltage, V_{c0} is the amplitude of carrier voltage and ω_c is the carrier frequency. In this study, ω_c is selected to be an order-of-magnitude larger than ω_{dr} (listed in TABLE i) to allow more room for the separation of frequencies of modulated signal.

Due to the band-width of the mechanical structure of micro-scanner, the carrier voltage is attenuated and the rotary motion θ can be modeled by a sinusoidal function with frequency half of ω_{dr} as

$$\theta = \theta_0\sin(\tfrac{\omega_{dr}}{2}t + \phi) \quad (17)$$

where θ_0 is amplitude of tilting motion, and ϕ is the phase of the tilting motion with respect to the driving voltage. By substitution of (17) into (15), and application of trigonometric identities, we have the $C_s(t)$ expressed as

$$C_s(t) = a_s\cos(\omega_{dr}t + 2\phi) + b_s \quad (18)$$

where $a_s = -\frac{a_c}{2}\theta_0^2$ and $b_s = \frac{a_c}{2}\theta_0^2 + b_c$.

In the AMDM amplification stage, the sensing current generated by the all the capacitance in the circuit under external voltage V is the derivative of the charge, therefore the output voltage of first stage V_{o1} can be expressed as

$$V_{o1} = R_f\frac{d}{dt}[(C_s(t) + C_p)V(t)] \quad (19)$$

where R_f is the feedback resistance. By applying the chain rule, we have:

$$V_{o1} = V(t)R_f\frac{dC_s(t)}{dt} + C_sR_f\frac{dV(t)}{dt} + C_pR_f\frac{dV(t)}{dt} \quad (20)$$

Substituting (16) into (20), and applying the chain rule, we have 6 components in the output V_{o1}:

$$\begin{cases} V_{o1} = V_1 + V_2 + V_3 + V_4 + V_5 + V_6 \\ V_1 = V_{dr0}R_f\frac{dC_s(t)}{dt}\sin(\omega_{dr}t) \\ V_2 = V_{c0}R_f\frac{dC_s(t)}{dt}\sin(\omega_c t) \\ V_3 = \omega_{dr}V_{dr0}R_fC_s(t)\cos(\omega_{dr}t) \\ V_4 = \omega_cV_{c0}R_fC_s(t)\cos(\omega_c t) \\ V_5 = \omega_{dr}V_{dr0}R_fC_p\cos(\omega_{dr}t) \\ V_6 = \omega_cV_{c0}R_fC_p\cos(\omega_c t) \end{cases} \quad (21)$$

Further derivation (Appendix, I.A) shows that V_1, V_3 and V_5 are composed of signal components with frequencies of ω_{dr}, $2\omega_{dr}$and DC, and therefore can be filtered out by a high pass filter with cut-off frequency be between $2\omega_{dr}$ and ω_c. On the other hand, V_2, V_4 and V_6 consists of signals with frequencies of ω_c and $\omega_c \pm \omega_{dr}$ can be retained by the high pass filter for subsequent processing, as illustrated in Fig. 3 (a).

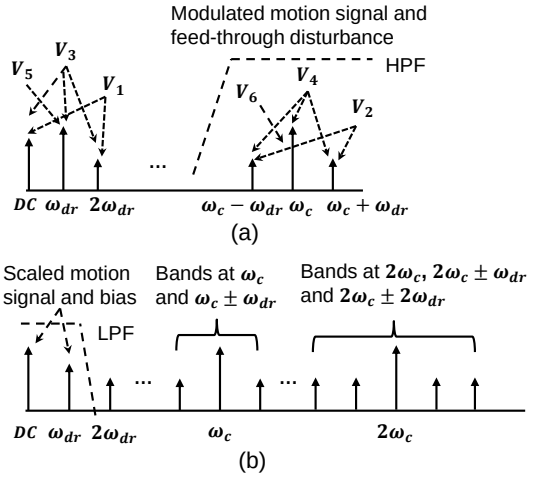

Fig. 3. (a) Illustration of frequency bands of output of amplification stage (V_{o1}) and separation of bands by high pass filter. (b) Illustration of demodulation of motion signal by envelope detector and low pass filter in frequency domain.

As shown in Appendix I.A, by selecting ω_c much larger than ω_{dr}, the magnitude of the side bands V_2 can be neglected compared to V_4. As ω_c is selected to be an-order-of-magnitude larger than that of ω_{dr}(TABLE i), it is safe to make this assumption and model V_{o2} as:

$$V_{o2} = a_{HPF}(V_4 + V_6) \quad (22)$$

`

where a_{HPF} is the gain of the high pass filter.

After the high pass filter, the capacitive sensing signal y_{cap} can be constructed using an envelope detector and one or more low pass filters as depicted in Fig. 2. The envelope detector consists of a diode, a resistor as load and the low pass filter(s). The output current of the diode can be modeled as a quadratic function of input voltage using a square-law function [20], therefore the voltage response of the envelope detector, V_{o3} can be modeled as

$$V_{o3} = a_d V_{o2} + b_d V_{o2}^2 \tag{23}$$

where a_d is the scale factor of envelope detector model, and b_d is the bias of the envelope detector. Substituting V_{o2} into (23) using (22), replacing V_4 and V_6 using (19), and letting $a_{o3} = a_{HPF} a_d \omega_c V_{c0} R_f$, $b_{o3} = b_d a_{HPF}^2 \omega_c^2 V_{c0}^2 R_f^2$, we have

$$V_{o3} = a_{o3}\cos(\omega_c t)(C_s + C_p) + b_{o3}\cos^2(\omega_c t)\left(C_s + C_p\right)^2 \tag{24}$$

By expanding the quadratic term (show in Appendix I.A), we obtain signal bands around $2\omega_c$ and ω_c, and signal bands at $2\omega_{dr}$, ω_{dr} and DC, as illustrated by Fig. 3 (b).

Next, by applying low pass filters with cut-off frequency slightly above ω_{dr} to V_{o3}, all the signals with frequency bands above ω_{dr} can be filtered out. By eliminating the term of $\cos(\omega_{dr} t + 2\phi)$ using (18), and lumping all coefficients together, we have

$$y_{cap}(t) = a_{cir} C_s(t) + b_{cir} \tag{25}$$

where $a_{cir} = a_{LPF} b_{o3}(b_s + C_p)$ is sensing circuit gain, and $b_{cir} = a_{LPF} b_{o3}(\frac{1}{4}a_s^2 - \frac{1}{2}b_s^2 + \frac{1}{2}C_p^2)$ is sensing circuit bias. Both of these parameters can be identified with experimental methods described in Section III and Section IV. The above derivation from (13) to (25) shows that the change of capacitance due to the tilting motion $C_s(t)$ can be modeled by a linear transformation of the measured signal y_{cap}.

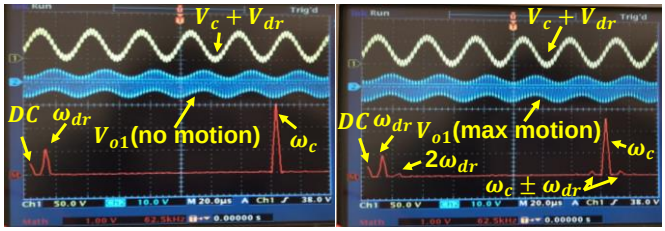

(a) (b)

Fig. 4. Experimentally measured input and output (with FFT) voltages at amplification stage. (a) measured V_{o1} with FFT with no rotatory motion excited. (b) measured V_{o1} with FFT with rotary motion excited at maximum amplitude. Signal of rotary motion observed to be carried at side bands with frequencies of $\omega_c \pm \omega_{dr}$.

As support of the model above for frequency bands, Fig. 4 and Fig. 5 show a group of representative input voltage and output voltages of each stage experimentally measured by a Tektronix TDS 3032C oscilloscope during the sensing circuit assembly process (see TABLE i). The output voltage response is analyzed by fast-Fourier-transformation (FFT) in real-time.

Fig. 4 (a) and (b) show two snapshots of the measured input voltage and V_{o1} (time domain and FFT) during a ω_{dr} sweep around resonance of the scanner. Fig. 4 (a) shows when the micro-scanner has no rotary motion, V_{o1} is largely composed of feed-through of input voltages (V_5, V_6 and bias voltage); whereas Fig. 4 (b) shows at the moment of the micro-scanner's rotary motion reaches its maximum amplitude, the sensing capacitance change induced by the motion is carried at sidebands at frequency of $\omega_c \pm \omega_{dr}$ (V_4) and can therefore be retained by high pass filter from lower frequency content.

Fig. 5 (a) shows the measured input voltage and V_{o3}, the FFT (up to 625 kHz) shows that the side bands after envelope detector matches the analysis and illustration at Fig. 3 (b). Fig. 5 (b) shows the measured y_{cap} after low pass filter. The sensing signal contains motion signal at frequency of ω_{dr} and bias voltage at DC.

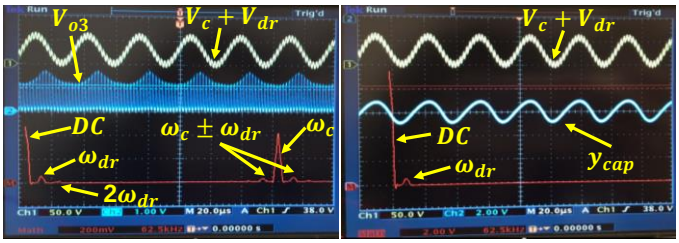

(a) (b)

Fig. 5. Experimentally measured input and output (with FFT) voltages at demodulation process. (a) measured V_{o3} with FFT with maximum rotary motion (b) measured y_{cap} with FFT with maximum rotary motion.

It is worth noting that although the above derivation is based on a quadratic capacitance model defined by (15), the relation characterized in in (25) is still valid when extended to a capacitance model characterized by a Gaussian function defined in (13). This is because the higher-order terms of θ^{2n} (n > 2) in (14) consists of signal components with relatively small magnitudes for $\theta < \theta_0$ and high frequency, and therefore consist of insignificant portion of signal after filtering.

On the other hand, using the Gaussian model from (13) to help to characterize the tail of the capacitance profile (see Fig. 7 (b)) is much needed in estimator development, not only because such a model is more precise when θ is larger [18], it also provides a bounded asymptotic value for C_s when θ approaches its maximum or minimum value, preventing $dC_s/d\theta$ from overflowing in the Jacobian matrix during the recursive updating in the EKF or UKF estimator.

Therefore, one can establish the overall measurement model in discrete-time domain by replacing $C_s(\theta)$ from (13) into (25) and assuming that an additive zero mean normally distributed noise, v_k, corrupts the measurement

$$y_{cap,k} = a_{cir}\left[C_0 e^{-\left(\frac{x_{1,k}}{\theta_0}\right)^2} + C_b\right] + b_{cir} + v_k \tag{26}$$

Denoting $h(\cdot)$ as the measurement model, we have

$$h(x_{1,k}) = a_{cir}\left[C_0 e^{-\left(\frac{x_{1,k}}{\theta_0}\right)^2} + C_b\right] + b_{cir} \tag{27}$$

The parameters of a_{cir}, b_{cir}, θ_0, C_0 and C_b can be identified experimentally by methods described in Section III and IV.

D. EKF and UKF formulation

With knowledge of non-linear dynamics of both the electrostatic micro-scanner and sensor model, both an EKF and

`

an UKF were implemented to estimate tilting motion; their performance is evaluated and presented in Section IV.

Both estimators deal with nonlinear models with normally-distributed noise. The main difference lies the approach used to calculate the mean and covariance of the states after propagation by the nonlinear models. The EKF perform a first order Taylor expansion of the non-linear models (aka Jacobian) around the *a priori* estimated states and is relatively easy to implement [21], whereas the UKF selects a minimal number of sigma points to estimate the *a priori* and *a posteriori* mean and covariance of states, and therefore leads to accuracy as high as a third order of Taylor expansion at a cost of greater implementation effort [22].

For the purpose of description of the two filters, we denote the superscript '–' for *a priori* terms, while the subscript k stands for k-th sampling instance. The state vector is defined to be $\boldsymbol{X} = [x_1 \quad x_2]^T$, where x_1 is angular position and x_2 is angular velocity. Having the most important components such as process model (Section II B) and measurement model (Section II C) described in detail, we present the rest of derivation of estimators only in high level due to the limit of page. The EKF algorithm is:

Algorithm 1: EKF

1. Project *a priori* state estimates

$$\widehat{\boldsymbol{X}}_k^- = g(\widehat{\boldsymbol{X}}_{k-1}, V_k), \quad \boldsymbol{P_k^-} = \boldsymbol{G_k P_{k-1} G_k^T} + \boldsymbol{Q}$$

2. Propagating measurement model

$$\hat{y}_{cap,k} = h(\hat{x}_{1,k}^-)$$

3. Project *a posteriori* state estimates

$$\boldsymbol{K}_k = \boldsymbol{P_k^- H_k^T}\left(\boldsymbol{H_k P_k^- H_k^T} + R\right)^{-1}$$

$$\widehat{\boldsymbol{X}}_{\boldsymbol{k}} = \widehat{\boldsymbol{X}}_{\boldsymbol{k}}^- + \boldsymbol{K_k}\left(y_{cap,k} - \hat{y}_{cap,k}\right), \quad \boldsymbol{P_k} = \boldsymbol{P_k^-} - \boldsymbol{K_k H_k^T P_k^-}$$

where $\widehat{\boldsymbol{X}}_{\boldsymbol{k}}^-$ is the *a priori* states estimation, $\boldsymbol{P_k^-}$ is the *a priori* error covariance matrix, $g(\cdot)$ is the process model defined in (10) and $h(\cdot)$ is the measurement model defined in (27), G_k and H_k are the Jacobian matrix of the process model and measurement model evaluated at *a priori* respectively, $\boldsymbol{Q}$ is the covariance matrix of process noise defined in (12), $\hat{y}_{cap,k}$ is the estimated measurement, $\boldsymbol{K_k}$ is the Kalman gain, R is covariance matrix of measurement noise, $\widehat{\boldsymbol{X}}_{\boldsymbol{k}}$ is the *a posteriori* states estimation and P_k is the *a posteriori* error covariance matrix.

The UKF algorithm is:

Algorithm 2: UKF

1. Set sigma points

$$\boldsymbol{X_{k-1}^{sig}} = \left\{\left(\widehat{\boldsymbol{X}}_{k-1}^i, W^i\right) \middle| i = 0 \ldots 2n_{aug}\right\}$$

2. Project *a priori* state estimates

$$\widehat{\boldsymbol{X}}_{\boldsymbol{k}}^{\boldsymbol{i},-} = g(\widehat{\boldsymbol{X}}_{\boldsymbol{k-1}}^{\boldsymbol{i}}), \quad \widehat{\boldsymbol{X}}_{\boldsymbol{k}}^- = \sum_{i=0}^{2n_{aug}} W^i\, \widehat{\boldsymbol{X}}_{\boldsymbol{k}}^{\boldsymbol{i},-}$$

$$\boldsymbol{P_{x,k}^-} = \sum_{i=0}^{2n_{aug}} W^i\left[\widehat{\boldsymbol{X}}_{\boldsymbol{k}}^{\boldsymbol{i},-} - \widehat{\boldsymbol{X}}_{\boldsymbol{k}}^-\right]\left[\widehat{\boldsymbol{X}}_{\boldsymbol{k}}^{\boldsymbol{i},-} - \widehat{\boldsymbol{X}}_{\boldsymbol{k}}^-\right]^T + \boldsymbol{Q}$$

3. Propagating measurement model

$$\hat{y}_{cap,k}^i = h(\hat{x}_{1,k}^{i,-}), \qquad \hat{y}_{cap,k} = \sum_{i=0}^{2n_{aug}} W^i \hat{y}_k^i$$

$$P_{y,k} = \sum_{i=0}^{2n_{aug}} W^i\left[\hat{y}_{cap,k}^i - \hat{y}_{cap,k}\right]\left[\hat{y}_{cap,k}^i - \hat{y}_{cap,k}\right]^T + R$$

4. Project *a posteriori* state estimates

$$\boldsymbol{P_{xy,k}} = \sum_{i=0}^{2n_{aug}} W^i\left[\widehat{\boldsymbol{X}}_{\boldsymbol{k}}^{\boldsymbol{i},-} - \widehat{\boldsymbol{X}}_{\boldsymbol{k}}^-\right]\left[\hat{y}_{cap,k}^i - \hat{y}_{cap,k}\right]^T + R$$

$$K_k = P_{xy,k} P_{y,k}^{-1}$$

$$\widehat{\boldsymbol{X}}_{\boldsymbol{k}}^{\boldsymbol{i}} = \widehat{\boldsymbol{X}}_{\boldsymbol{k}}^{\boldsymbol{i},-} + K_k(y_{cap,k}^i - \hat{y}_{cap,k}^i), \quad \boldsymbol{P_{x,k}} = \boldsymbol{P_{x,k}^-} + K_k P_{y,k} K_k^T$$

where $\boldsymbol{X_{k-1}^{sig}}$ is a set of sigma vectors and their associated weights, with $\widehat{\boldsymbol{X}}_{k-1}^i$ a sigma vector and W^i is its associated weight. The number of augmented sigma vectors n_{aug} is determined by the dimension of the state, W^i is set to be $\frac{\lambda}{(\lambda+L)}$ ($i = 0$) or $\frac{1}{2(\lambda+L)}$ ($i = 1, 2 \ldots 2n_{aug}$), and $L = 1 + 2n_{aug}$ [22]. $\widehat{\boldsymbol{X}}_{\boldsymbol{k}}^{\boldsymbol{i},-}$ is the sigma vector transformed by the process model, $\widehat{\boldsymbol{X}}_{\boldsymbol{k}}^-$ is the mean of *a priori* states estimation, $\boldsymbol{P_{x,k}^-}$ is the a priori error covariance matrix, $\boldsymbol{Q}$ is the covariance matrix of process noise, $\hat{y}_{cap,k}^i$ is the estimated measurement with the i-th sigma vector, $\hat{y}_{cap,k}$ is the estimated measurement, $P_{y,k}$ is the covariance of measurement estimation, $\boldsymbol{P_{xy,k}}$ is the cross covariance between estimated states and the measurement, R is the covariance matrix of measurement noise, $\widehat{\boldsymbol{X}}_{\boldsymbol{k}}^{\boldsymbol{i}}$ is the mean of the *a posteriori* states estimates and $\boldsymbol{P_{x,k}}$ is the *a posteriori* error covariance matrix.

III. EXPERIMENTS

This section describes the experimental set-up and the experiments for process model and measurement model identification and estimator performance evaluation.

A. Experimental set-up

The experimental set up is depicted in a schematic shown as Fig. 6 (a). Two command voltages (driver and carrier) were added using a summing amplifier and then amplified by a TEGAM 2340 amplifier with 20 times amplification. The amplified amplitude modulated driving voltage was fed into the single-axis electrostatic micro-scanner (see Fig. 1) to drive it near its resonant frequency.

It is worth noting that while the micro-scanner is more commonly excited using square wave driving voltage [23], it is also possible to drive the micro-scanner with a sinusoidal voltage [14]. One difference between the two choices that cannot be ignored in this study is that a square voltage introduces more frequency bands. For this study, we choose to use a sinusoidal voltage input in order to isolate the frequency bands introduced by the driving voltage, with modest reduction in amplitude.

The tilting motion of the micro-scanner was recorded by two different sensing systems. The first was the capacitive sensing circuit described in Section II-C (Fig. 2), which transduced the

motion into the signal y_{cap}. The second system was an optical sensing stage, which provided ground truth angular position measurement as a voltage signal y_{PSD}.

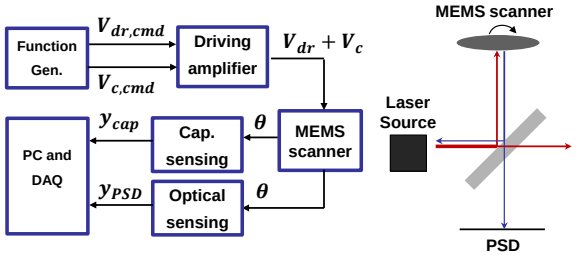

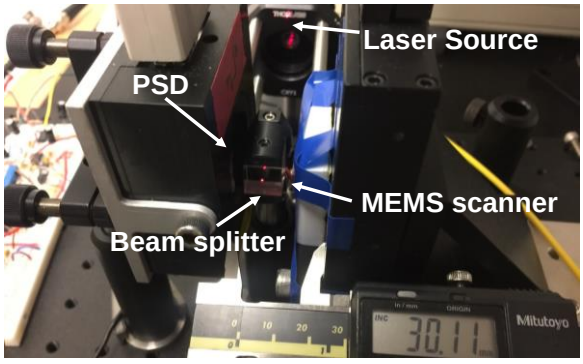

Fig. 6. (a) Schematic of experimental set-up. (b) A schematic of the optical sensing system used, it provided ground truth measurement of the tilting motion. A beam splitter is used to deflect the laser beams from the source and from the MEMS scanner in order to reduce the distortion generated. (c) A photo of optical sensing system used in the study.

The schematic of the optical sensing stage is depicted in Fig. 6 (b) and the actual set-up is shown in Fig. 6 (c). it consisted of an ON-TRAK PSM 2-10 position sensing detector (PSD), a BS004 Thorlabs beam splitter, and a OZ Optics FODL-42.5U 635 nm wavelength laser source. During the measurement, a laser beam was directed to the beam splitter, and half of the laser was reflected and directed to the mirror surface of the MEMS scanner at a 0° incidence angle. With the MEMS scanner driven by external stimulus, the mirror surface rotates and reflects the incoming beam to the same beam splitter, and the reflected beam is split by the beam splitter again before the final portion of the beam being received by the PSD and converted into a voltage signal y_{PSD}. y_{PSD} was converted into angular displacement using geometry relation and PSD gains.

B. Experimental procedures

To identify the parameters related to the models and to evaluate estimators' performance, a set of ringdown experiments and a set of steady-state responses experiments were performed, and the experimental settings are summarized in TABLE i.

The first set of ringdown experiments was done to identify the micro-scanner's dynamic model and capacitance profile [9]. The driving voltage was swept in frequency from high to low near 31.10 kHz to allow the scanner reach to maximum tilting amplitude. After the tilting motion stabilized, the driving voltage was switched from AC to DC to allow the scanner to free oscillate with a constant bias voltage applied. During ring-down tests, V_{o1} (see Fig. 2) and y_{PSD} were recorded using a NI PCI 6115 DAQ with 12 bit resolution and 5 MHz sampling rate. A customized LabVIEW program was developed to send command voltage and log data.

TABLE I

EXPERIMENTAL SETTINGS FOR ELECTROSTATIC MICRO-SCANNER

Symbol	Description	Value
V_{dr0}	Amplitude of driving voltage	30 V (0 V to 60V)
V_{c0}	Amplitude of carrier voltage	6 V
f_{res}	Resonant frequency of micro-scanner	15.50 kHz
f_{dr}	Frequency of driving voltage	31.11 to 31.50 kHz
f_c	Frequency of carrier voltage	500 kHz
R_f	Feedback resistors	17.86 kohm
V_{bias}	Bias voltage	23.76 V
f_{HP}	HPF cut-off frequency	482 kHz
f_{LP}	LPF cut-off frequency	40.8 kHz
f_{ED}	Envelop detector LPF cut-off	41.1 kHz

The second set of experiments consisted of frequency sweeps of steady-state responses of micro-scanner, and the measurements were used to identify remaining model parameters and evaluate the estimators' performance. In these experiments, the scanner was excited with amplitude-modulated driving voltages at a set of frequencies near resonance, with y_{cap}, y_{PSD} and driving voltages recorded. In total a set of 15 frequencies ranging from 31.11 kHz to 31.50 kHz were tested. During steady state frequency sweeps, a dual channel function generator was used to provide command carrier voltage and provide voltage to the driving circuit, while an Agilent InfinitiVision DSO-X 2024A oscilloscope was used to record the measurements.

IV. RESULTS AND DISCUSSION

In this section, the experimental results are processed and presented. First, a system identification is performed. Second, the performance of estimators are defined and evaluated. At last, the effect of different errors in phase estimation on the quality of image reconstruction is demonstrated in a post-processed in-vivo mouse colon image.

A. System identification

The system identification process involves three independent steps: first, identifying the parameters of Gaussian capacitance model defined in (13), θ_0, C_0 and C_b; second, identifying the coefficients of overall circuit gains defined in (25), a_{cir} and b_{cir}; third, identifying the actuator model.

TABLE II

IDENTIFIED PARAMETERS OF MODELS AND ESTIMATORS

Symbol	Description	Value
J	Moment of inertia	1.15×10^{-14} kg m^2
k	Spring constant	1.10×10^{-4} N m
b_v	Viscous damping coefficient	5.95×10^{-12} N m/s
Q_θ	Noise variance of angular position	10^{11} m/s^2
θ_0	Nominal angular displacement	0.2 rad
C_0	Nominal capacitance	5.71 pF
C_b	Parasitic capacitance	9.79 pF
a_{cir}	Circuit scale factor	-0.3574 V/pF
b_{cir}	Circuit bias	6.3945 V
R	Covariance of measurement noise	1.92×10^{-4} V^2

`

The second step uses a subset of result from the steady state frequency sweep experiments. The ground truth $\theta(t)$ is used as the input to the $C_s(\theta)$ model identified to obtain $C_s(t)$. Then by treating $C_s(t)$ and correspondingly observed $y_{cap}(t)$ as knowns, a_{cir} and b_{cir} can be solved by least square methods

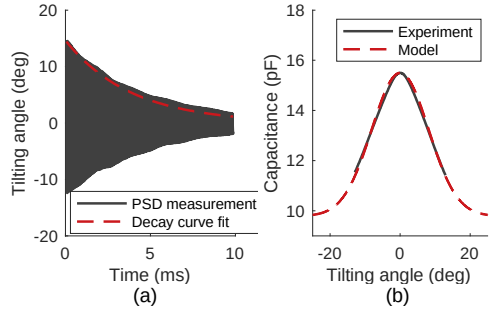

Fig. 7. (a) Measurement of ringdown test and fitted decay curve for actuator model parameter identification. (b) Experimentally identified capacitance profile vs. modeled capacitance profile. The tail of capacitance profile vs. larger angle modeled improves the numerical stability of estimator implementation.

The covariance of measurement noise is identified by measuring the circuit output with zero tilting motion. The identified parameters are summarized in TABLE ii.

The actuator model was identified by first calculating the moment of inertia, J, from the dimensions of the micro-scanner, and then fitting the decay curve of the experimentally measured ringdown trajectory using a linear viscous damping and spring constant [9] as illustrated in Fig. 7 (a).

B. Estimators performance comparison

In this section, the performance of estimators are defined and evaluated. First, three estimation schemes are selected for comparison: actuator model alone (ACM), EKF incorporating actuator and measurement model (EKF), UKF incorporating actuator model and measurement model (UKF), and the performance metrics are calculated against experimentally measured ground truth (EXP).

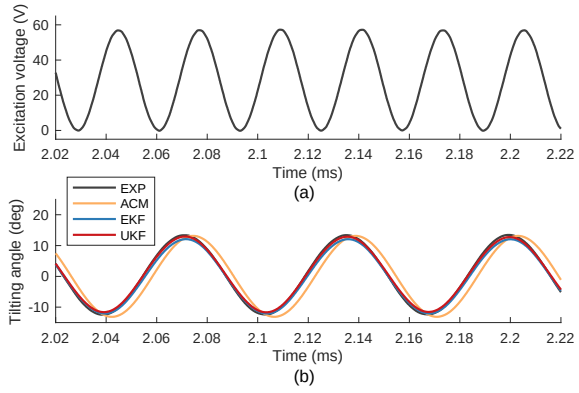

Fig. 8. (a) Experimentally measured driving voltage (carrier filtered for better presentation). (b) Tilting angle measured (EXP) or estimated by actuator model (ACM), extended Kalman filter (EKF) and unscented Kalman filter (UKF).

Second, the root-mean-square error (RMSE) of angular position and RMSE of phase shift of the micro-scanner are selected as performance metrics. The phase shift is defined as the difference of the timing between the peak value of an angular displacement and the prior peak value of the driving voltage. The performance of estimator is evaluated using the subset of steady state frequency sweep experiments complementary of the subset used for system identification.

Fig. 8 shows a representative excitation voltage (without modulation) (a) and resultant tilting motion (b) against time. As illustrated, both the EKF and UKF show less error in phase shift compared to the ACM, and therefore have more accurate angular position estimation.

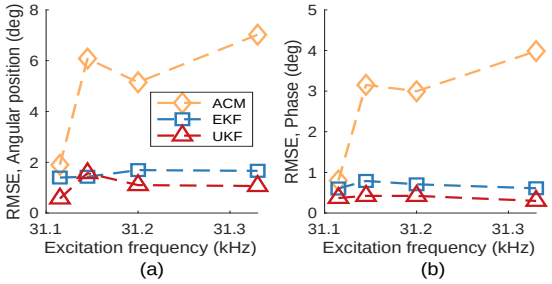

Fig. 9. (a) RMSE of angular position of MEMS device measured by optical system (EXP) and estimated by actuator model (ACM), extended Kalman filter (EKF) and unscented Kalman filter (UKF). (b) RMSE of phase shift of tilting angle measured and estimated respectively.

Fig. 9 shows the RMSE of angular position (a) and RMSE of phase shift (b) of different estimators. Both EKF and UKF provide significantly more accurate angular position and phase shift estimation than ACM across the tested frequencies.

The average RMSE for the testing data set is also quantified and listed in TABLE iii. For perspective, the RMSE of angular position is also computed as the percentage of the peak-to-peak amplitude of the tilting motion. The higher estimation accuracy of the UKF over EKF is likely due to the UKF being more accurate in estimating mean and covariance of states propagated by non-linear models than the EKF. The error in phase estimation using the UKF reaches the target accuracy of 0.38 degrees derived in Section II A given the exemplary setting of 300 × 300 resolution and single-pixel index shift.

TABLE III

RMSE OF ANGULAR POSITION AND PHASE SHIFT BY ESTIMATORS

Estimator	**RMSE Angular position (deg)**	**RMSE phase shift (deg)**
ACM	2.89	2.73
EKF	0.89 (reduced 69.2%)	0.68 (reduced 75.1%)
UKF	0.62 (reduced 78.5%)	0.38 (reduced 86.1%)

It is worth noting that according to (7), the target phase shift accuracy varies with image resolution and number of pixel index shift. For instance, the target phase shift accuracy would be 0.76 deg if two-pixel index shift were allowed, and EKF's accuracy would therefore be qualified. In the case of higher image resolution, meaningful improvement in image quality can still be made with UKF or EKF compared to without using estimator or using ACM, as demonstrated in Section IV C. In summary, it is advised to choose type of estimators to balance target estimation accuracy and implementation effort.

`

C. Effect of phase estimation error on mouse colon image

In this subsection, we demonstrate the effect of different errors in phase estimation on the quality of image reconstruction. We used a reconstructed in-vivo mouse colon image with 400 × 400 resolution and 250 × 250 μm FOV as a representative example. The pixels on the image were sampled in a Lissajous pattern with a dual-axis MEMS scanner with scanning frequencies 27.68 kHz for x-axis and 6.54 kHz for y-axis. In the demonstration, only the phase estimation of the fast axis (x-axis) was varied to match the single-axis phase estimation reported in TABLE iii. For reader's reference, single-pixel index shift requires accuracy of 0.29 deg in phase shift estimation, whereas two-pixel index shift requires 0.57 deg.

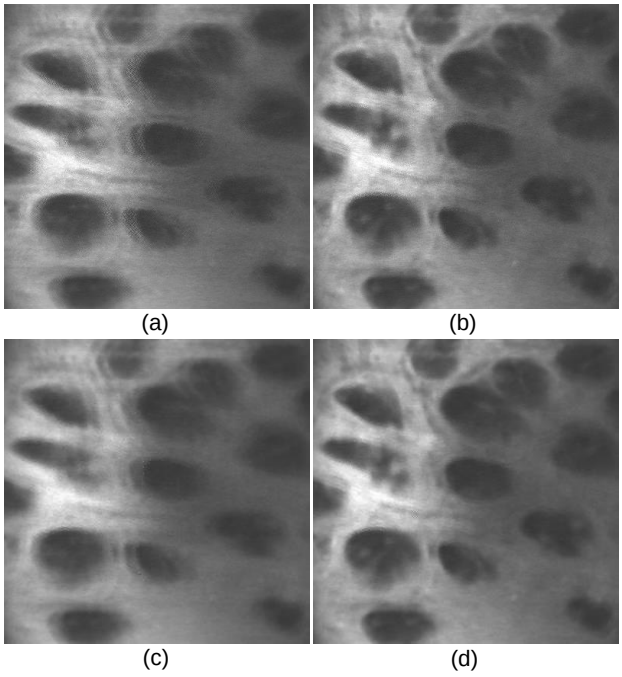

Fig. 10. Comparison of reconstructed in-vivo images of mouse colon with various phase adjustment in motion generated by x-axis. (a) Without phase adjustment. (b) With near optimal phase adjustment by tuning. (c) With phase adjustment equivalent to ACM performance. (d) With phase adjustment equivalent to UKF performance.

The image is first reconstructed with phases identified during laboratory calibration prior to the in-vivo experiments in both axes (380.143 degree for x-axis and 370.116 degree for y-axis), shown as Fig. 10(a). The image has noticeable blur as the phase has drifted due to the change of micro-scanner dynamics inside the mouse's colon. Secondly, a near-optimal phase shift in x-axis is estimated (379.398 degree for x-axis) by manual tuning and the resultant image is shown as Fig. 10 (b). This is done due to the absence of ground truth measurement of the scanner's motion inside the mouse body, and is only for the purpose of serving as a benchmark. Then, errors equivalent to the performance of the estimators were introduced in the x-axis phase estimation during the reconstruction of the corresponding images (0.38 degree for UKF and 2.73 degree for ACM) to emulate the best case single-axis phase estimation with (UKF) and without (ACM) capacitive sensor measurement. The resultant images are shown as Fig. 10 (c) and (d) respectively. The level of accuracy of phase estimation equivalent to UKF's performance lead to noticeable improvement in blur reduction compared to that of ACM, even when phase correction is only applied to the fast axis.

V. Conclusion

Accurate estimation of phase shift of the scanning trajectory of MEMS micro-scanners is necessary to avoid blur of image reconstructions in endoscopy applications. To overcome this issue, we present a method to estimate tilting motion of an electrostatic micro-scanner using shared electrodes for driving and sensing. The method includes an AMDM circuit design to separate feedthrough generated by the high driving voltage. Novelties of the proposed sensor and estimator implementation include a process model based on non-linear parametric dynamics of micro-scanner and a non-linear sensor model including a Gaussian based capacitance model and a circuit model based on frequency bands analysis. Both EKF and UKF estimators are implemented, and estimation performance are examined and compared with experimental results.

The results show that the UKF achieved 0.38 degree RMSE in phase shift estimation, while the EKF achieved 0.68 degree RMSE in phase estimation. Compared to the estimator ACM that does not use sensing signal and Kalman filters, the estimation error has been reduce by as much as 86.1% in phase shift and 78.5% in angular position estimation by UKF.

Recommended future work is to extend and implement the method in a 2D micro-scanner while maintaining the same level of the phase shift estimation error.

Appendix

A. Derivation of frequency bands of sensing circuits

In this section, we show the omitted derivation of the frequency bands of output response of each stage (V_{o1}, V_{o2}, V_{o3}, y_{cap}) in detail. First, starting from (21) and expanding each voltage component in the output V_{o1} by replacing $C_s(t)$ defined in (18):

$$V_1 = V_{dr0}R_f\frac{dC_s(t)}{dt}\sin(\omega_{dr}t)$$
$$= V_{dr0}R_f[-a_s\omega_{dr}\sin(\omega_{dr}t+2\phi)]\sin(\omega_{dr})$$
$$= \tfrac{1}{2}a_sV_{dr0}R_f\omega_{dr}[\cos(2\omega_{dr}+2\phi)-\cos(2\phi)] \quad (28)$$

$$V_2 = V_{c0}R_f\frac{dC_s(t)}{dt}\sin(\omega_c t)$$
$$= -a_sR_fV_{c0}\omega_{dr}\sin(\omega_{dr}t+2\phi)\sin(\omega_c t)$$
$$= \tfrac{1}{2}a_sR_fV_{c0}\omega_{dr}[\cos((\omega_c-\omega_{dr})\,t-2\phi)-\cos((\omega_c+\omega_{dr})t+2\phi)] \quad (29)$$

$$V_3 = \omega_{dr}V_{dr0}R_fC_s(t)\cos(\omega_{dr}t)$$
$$= \omega_{dr}V_{dr0}R_f[a_s\cos(\omega_{dr}t+2\phi)+b_s]\cos(\omega_{dr}t)$$
$$= \tfrac{1}{2}a_sV_{dr0}\omega_{dr}\cos(2\omega_{dr}+2\phi)+b_s\cos(\omega_{dr}t)+\tfrac{1}{2}a_sV_{dr0}\omega_{dr}\cos(2\phi) \quad (30)$$

`

$$V_4 = \omega_c V_{c0} R_f C_s(t) \cos(\omega_c t)$$

$$= \omega_c V_{c0} R_f [a_s \cos(\omega_{dr} t + 2\phi) + b_s] \cos(\omega_c t)$$

$$= a_s \omega_c V_{c0} R_f \left[\cos\left((\omega_c - \omega_{dr})t - 2\phi\right) + \cos\left((\omega_c + \omega_{dr})t + 2\phi\right)\right] + \omega_c V_{c0} R_f b_s \cos(\omega_c t) \quad (31)$$

$$V_5 = \omega_{dr} V_{dr0} R_f C_p \cos(\omega_{dr} t) \quad (32)$$

$$V_6 = \omega_c V_{c0} R_f C_p \cos(\omega_c t) \quad (33)$$

By collecting the frequency term in each component, we obtain a set of frequency bands illustrated in Fig. 3 (a).

To derive the composition of V_{o2}, first denote the side bands of V_4 at frequencies of $\omega_c \pm \omega_{dr}$ as

$$V_{4\_side} = \omega_c a_s V_{c0} R_f \cos(\omega_{dr} t + 2\phi) \cos(\omega_c t) \quad (34)$$

By comparing V_{4_side} to V_2, one can see that as long as ω_c is much larger than ω_{dr}, V_{4_side} is dominant in terms of magnitude. Therefore, a simplification is made to model V_{o2}:

$$V_{o2} = a_{HPF}(V_4 + V_6) \quad (35)$$

To analyze V_{o3}, we replace C_s in (24) with (18) and obtain:

$$V_{o3} = \frac{1}{8} b_{o3} a_s^2 [\cos(2(\omega_c - \omega_{dr})t - 4\phi) + \cos(2(\omega_c + \omega_{dr})t + 4\phi)] + b_{o3}\left(\frac{1}{4}a_s^2 + \frac{1}{2}b_s^2 + C_p b_s + \frac{1}{2}C_p^2\right)\cos(2\omega_c t) + a_s b_{o3} b_s\left[\cos\left((2\omega_c - \omega_{dr})t - 2\phi\right) + \cos\left((2\omega_c + \omega_{dr})t + 2\phi\right)\right] + a_s\left(\frac{1}{2}a_{o3} + b_{o3}b_s + b_{o3}C_p\right)\left[\cos\left((\omega_c - \omega_{dr})t - 2\phi\right) + \cos\left((\omega_c + \omega_{dr})t + 2\phi\right)\right] + a_{o3}\left(b_s + C_p\right)\cos(\omega_c t) + \frac{1}{4} b_{o3} a_s^2 \cos(2\omega_{dr} t + 4\phi) + a_s b_{o3}\left(b_s + C_p\right)\cos(\omega_{dr} t + 2\phi) + b_{o3}(\frac{1}{4}a_s^2 + \frac{1}{2}b_s^2 + \frac{1}{2}C_p^2 + b_s C_p) \quad (36)$$

The frequency bands in V_{o3} are around $2\omega_c$, ω_c, $2\omega_{dr}$, ω_{dr} and DC, as illustrated in Fig. 3 (b).

By applying low pass filters with cut-off frequency slightly above ω_{dr} to V_{o3}, all the signals with frequency bands above ω_{dr} can be filtered out. Replacing the term of $\cos(\omega_{dr} t + 2\phi)$ using (18), we have y_{cap} as

$$y_{cap} = a_{LPF} a_s b_{o3}\left(b_s + C_p\right)\cos(\omega_{dr} t + 2\phi) + a_{LPF} b_{o3}\left(\frac{a_s^2}{4} + \frac{b_s^2}{2} + \frac{C_p^2}{2} + C_p b_s\right) \quad (37)$$

where a_{LPF} is the gain of the low pass filter. (37) can be re-written as (15) by letting $a_{cir} = a_{LPF} b_{o3}(b_s + C_p)$ to be the sensing circuit gain, and $b_{cir} = a_{LPF} b_{o3}(\frac{1}{4}a_s^2 - \frac{1}{2}b_s^2 + \frac{1}{2}C_p^2)$ to be the sensing circuit bias. Replace $C_s(t)$ using model defined in (13), we have

$$y_{cap}(t) = a_{cir}(C_0 e^{-\left(\frac{\theta}{\theta_0}\right)^2} + C_b) + b_{cir} \quad (38)$$

(38) can then be expressed in discretized time domain measurement model, as defined in (26)

REFERENCES

[1] S. T. Holmstrom, U. Baran and H. Urey, "MEMS Laser Scanners: A Review," *Journal of Microelectromechanical Systems*, vol. 23, no. 2, pp. 259 - 275, 2014.

[2] Z. Qiu and W. Piyawattanametha, "MEMS-Based Medical Endomicroscopes," *IEEE Journal of Selected Topics in Quantum Electronics*, vol. 21, no. 4, 2015.

[3] X. Duan, H. Li, J. Zhou, Q. Zhou, O. R. Kenn and T. D. Wang, "Visualizing epithelial expression of EGFR in vivo with distal scanning side-viewing confocal endomicroscope," *Scientific reports*, p. 37315, 2016.

[4] X. Duan, H. Li, Z. Qiu, B. P. Joshi, A. Pant, A. Smith, K. Kurabayashi, K. R. Oldham and T. D. Wang, "MEMS-based multiphoton endomicroscope for repetitive imaging of mouse colon," *Biomedical optics express*, vol. 6, no. 8, pp. 3074-3083, 2015.

[5] U. Hofmann, J. Janes and H.-J. Quenzer, "High-Q MEMS resonators for laser beam scanning displays," *Micromachines*, vol. 3, no. 2, pp. 509 - 528, 2012.

[6] G. Stemme, "Resonant silicon sensors," *Journal of Micromechanics and Microengineering*, vol. 1, no. 2, p. 113, 1991.

[7] C. Drabe, D. Kallweit, A. Dreyhaupt, J. Grahmann, H. Schenk and W. Davis, "Bi-resonant scanning mirror with piezoresistive position sensor for WVGA laser projection systems," in *SPIE MOEMS-MEMS*, San Francisco, 2012.

[8] U. Baran, D. Brown, S. Holmstrom, D. Balma, W. O. Davis, P. Muralt and H. Urey, "Resonant PZT MEMS scanner for high-resolution displays," *Journal of Microelectromechanical Systems*, vol. 21, no. 6, pp. 1303 - 1310, 2012.

[9] R. Schroedter, M. Roth, . K. Janschek and T. Sandner, "Flatness-based open-loop and closed-loop control for electrostatic quasi-static microscanners using jerk-limited trajectory design," *Mechatronics*, 2017.

[10] Y. Chen, E. E. Aktakka, J.-K. Woo and K. Oldham, "Threshold sensing signal construction from a capacitive sensor for MEMS gyroscope calibration," in *IEEE International Conference on Advanced Intelligent Mechatronics (AIM)*, Banff, 2016.

[11] Y. Chen, E. E. Aktakka, J.-K. Woo, K. Najafi and K. R. Oldham, "On-chip capacitive sensing and tilting motion estimation of a micro-stage for in situ MEMS gyroscope calibration," *Mechatronics*, 2018.

[12] B. Edamana, Y. Chen, D. Slavin, E. E. Akatakka and K. R. Oldham, "Estimation with threshold sensing for gyroscope calibration using a piezoelectric microstage," *IEEE Transactions on Control Systems Technology*, vol. 23, no. 5, pp. 1943 - 1951, 2015.

[13] Y. Chen, H. Li, Z. Qiu, T. D. Wang and K. R. Oldham, "Improved Extended Kalman Filter Estimation using Threshold Signal Detection with a MEMS Electrostatic Micro-Scanner," *IEEE Transactions on Industrial Electronics*, 2019.

[14] A. A. Trusov and A. M. Shkel, "Capacitive detection in resonant MEMS with arbitrary amplitude of motion," *Journal of micromechanics and microengineering*, vol. 17, no. 8, p. 1583, 2007.

[15] B. Cagdaser, A. Jog, M. Last, B. S. Leibowitz, L. Zhou, E. Shelton, K. S. Pister and B. E. Boser, "Capacitive sense feedback control for MEMS beam steering mirrors," in *Solid-state Sensor, Actuator and Microsystems Workshop*, Hilton Head Island, 2004.

[16] A. C.-L. Hung, H. Y.-H. Lai, T.-W. Lin, S.-G. Fu and M. S.-C. Lu, "An electrostatically driven 2D micro-scanning mirror with capacitivesensing for projection display," *Sensors and Actuators A: Physical*, vol. 222, no. 1, pp. 122-129, 2015.

[17] H. Lin, T.-W. Lin, A. C.-L. Hung and M. S.-C. Lu, "A bi-axial capacitive scanning mirror with closed-loop control," in *IEEE Micro Electro Mechanical Systems (MEMS)*, Belfast, 2018.

[18] W. Shahid, Z. Qiu, X. Duan, L. Haijun, T. D. Wang and R. K. Oldham, "Modeling and Simulation of a Parametrically Resonant Micromirror With Duty-Cycled Excitation," *Journal of Microelectromechanical Systems*, pp. 1440 - 1453, 2014.

[19] C. Ataman and U. Hakan, "Modeling and characterization of comb-actuated resonant microscanners," *Journal of Micromechanics and Microengineering*, vol. 16, no. 1, 2005.

[20] L. E. Frenzel, Principles of electronic communication systems, New York: McGraw-Hill Education, 2007.

[21] G. Welch and G. Bishop, "An introduction to the Kalman filter,"

`

1995. [Online]. Available: http://byron.soe.ucsc.edu/projects/SeaSlug/Documents/Publications/Kalman%20Filtering/An%20Introduction%20to%20the%20Kalman%20Fiter2.pdf. [Accessed 2019].

[22] E. A. Wan and R. v. d. Merwe, "The unscented Kalman filter for nonlinear estimation," in *Adaptive Systems for Signal Processing, Communications, and Control Symposium*, Lake Louise, 2000.

[23] H. Schenk, P. Dürr, T. Haase, D. Kunze, U. Sobe, H. Lakner and H. Kück, "Large deflection micromechanical scanning mirrors for linear scans and pattern generation," *IEEE Journal of Selected Topics in Quantum Electronics*, vol. 6, no. 5, pp. 715 - 722, 2000.

Yi Chen received the B.S. degrees in mechanical engineering from the University of Michigan, Ann Arbor, MI, USA and Shanghai Jiao Tong University, Shanghai, China in 2010. He received a Master's degree in mechanical engineering in 2012, and a Master's degree in electrical engineering and a Ph.D. degree in mechanical engineering both in 2018 from the University of Michigan.
He is currently an software engineer with Midea Emerging Technology Center. His research interests include signal processing, computer vision and robotics.

Miki Lee received the B.S.E. degree in aerospace engineering from the University of Michigan, Ann Arbor, USA, in 2015, and the M.E. degree in space engineering from the University of Michigan, Ann Arbor, USA, in 2016.
Since 2016, she has been a Research Lab Specialist Associate with the Department of Internal Medicine, University of Michigan. Her research interests include the development of MEMS-based endomicroscopy imaging system and MEMS sensor design.

Mayur Bhushan Birla received the B.Tech. degree in mechanical engineering from Visvesvaraya National Institute of Technology, Nagpur, India in 2011 and the M.E. mechanical engineering from Indian Institute of Science (IISc), Bangalore, India in 2015. He is currently pursuing the M.S. in electrical engineering and the Ph.D. in mechanical engineering at University of Michigan, Ann Arbor, USA.
From 2011 to 2013, he was a Systems Engineering at BrahMos aerospace private limited, India. His research interest includes development of two photon endomicroscopy system compatible with commercially used endoscopes.
Mr. Mayur is recipient of 'Best student' in mechanical engineering at IISc, Bangalore and member of honor societies Tau Beta Pi, and Phi Kappa Phi.

Haijun Li received the Ph.D. degree in microelectronics and solid-state electronics from Jilin University, Changchun, China, in 2007. He held a post-doctoral position at Nanyang Technology University, Singapore, from 2008 to 2011. He was a Senior Engineer at the Hebei Semiconductor Research Institute, Shijiazhuang, China, from 1997 to 2008.
He is currently a Research Investigator with the University of Michigan, Ann Arbor, MI, USA, where he is involved in the development of MEMS-based endomicroscope. His research interests include MEMS, uncooled infrared detectors, epi-MEMS technology, and wafer level packaging technologies.

Gaoming Li received the Ph.D. degree in Optics from Xiamen University, Xiamen, Fujian, China in 2011. He received post-doctoral training at the Nanyang Technological University, Singapore, from 2014 to 2015, and the University of Michigan, Ann Arbor, MI, USA from 2015 to 2017.
He is currently a research investigator with the University of Michigan. His research interests include optical endomicroscopy, photoacoustic, optical design and speckle.

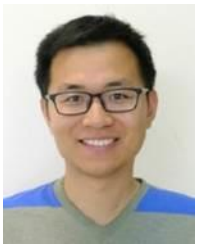

Xiyu Duan received the B.S degree in electrical engineering from Hong Kong University of Science and Technology, Hong Kong, China, in 2010, and the Ph.D. degree in biomedical engineering from the University of Michigan, Ann Arbor, MI, USA, in 2016.

His research focued on MEMS based fiber endomicroscopes to for real time optical biopsy. He is currently an hardware engineer at Apple Inc.

Thomas D. Wang received the B.S. degree in mathematics and physics from Harvey Mudd College, Claremont, CA, USA, in 1985, and the Ph.D. degree in medical engineering and medical physics from the Massachusetts Institute of Technology, Cambridge, MA, USA, in 1996.
He is currently a Professor of Medicine, Biomedical Engineering, and Mechanical Engineering at the University of Michigan and the H. Marvin Pollard Collegiate Professor of Endoscopy Research. He has developed a number of microsystems-based technologies to perform scanning and actuation for high speed imaging with large working distance in endomicroscopy. His research interests are in the field of biomedical optics, multiplexed detection, and molecular imaging.

Kenn R. Oldham received the B.S. degree in mechanical engineering from Carnegie Mellon University, Pittsburgh, PA, USA, in 2000, and the Ph.D. degree in mechanical engineering from the University of California at Berkeley, Berkeley, CA, USA, in 2006.
He is currently an Associate Professor of Mechanical Engineering at the University of Michigan. His research focuses on the intersection of control systems and micro-scale sensing and actuation, with interests in design for controllability, optimal and robust control, microsystem estimation and identification, and novel sensor and actuator design. Applications include terrestrial micro-robotics, endoscopic microscopy, and inertial and physiological sensing.